iScience

CellPress

Article

Solid-State, Low-Cost, and Green Synthesis and Robust Photochemical Hydrogen Evolution Performance of Ternary $TiO_2/MgTiO_3/C$ Photocatalysts

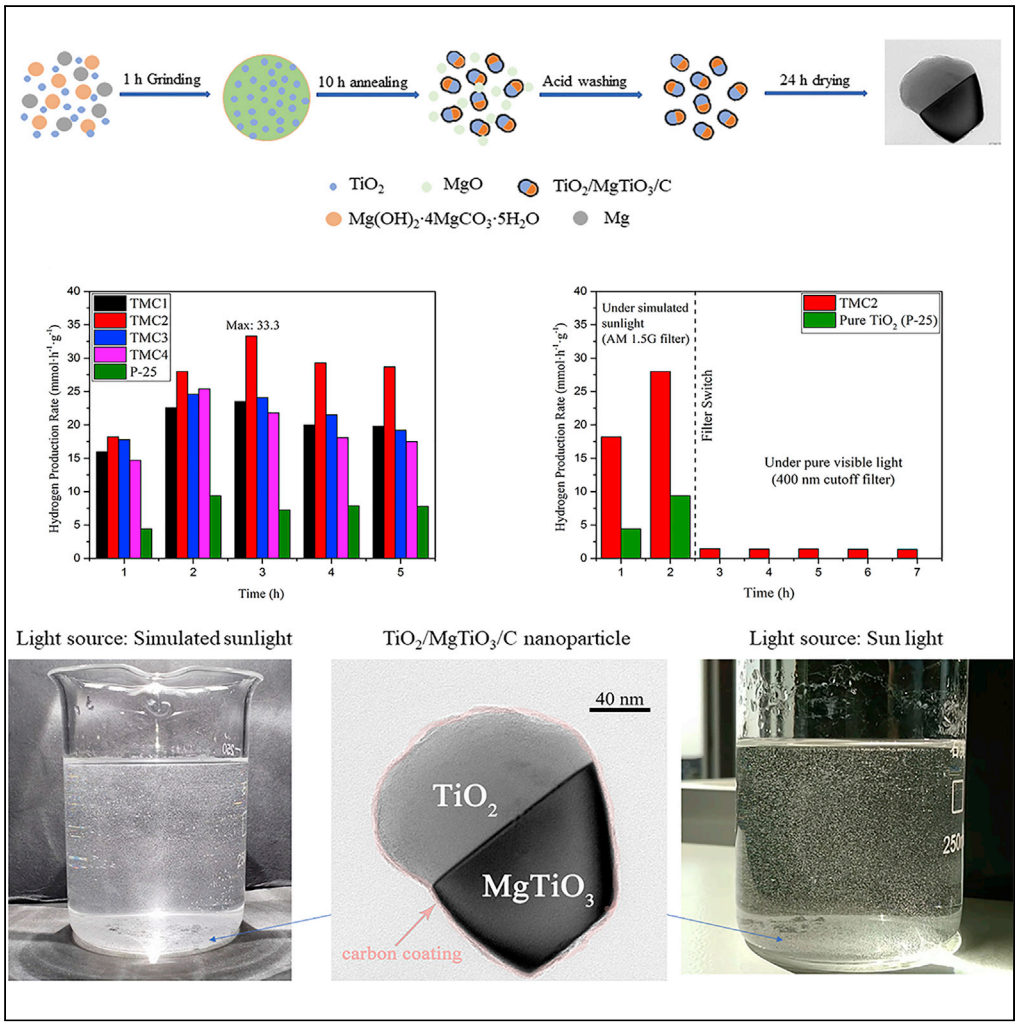

Zhongmei Yang, Yunhong Jiang, Wei Zhang, ..., Jiuren Yin, Ping Zhang, Hean Luo

yhding@xtu.edu.cn (Y.D.)
zhangp@xtu.edu.cn (P.Z.)

HIGHLIGHTS

The synthetic process does not involve any organic solvents and hazardous by-products

The optimal sample shows a H_2 evolution rate of 33.3 $mmol \cdot h^{-1} \cdot g^{-1}$ under one sunlight

The optimal sample keeps a H_2 evolution rate of 1.46 $mmol \cdot h^{-1} \cdot g^{-1}$ under visible light

Uniform carbon layer was ingeniously deposited on the surface of photocatalysts

Yang et al., iScience 14, 15–26
April 26, 2019
https://doi.org/10.1016/j.isci.2019.03.009

iScience

CellPress

Article

Solid-State, Low-Cost, and Green Synthesis and Robust Photochemical Hydrogen Evolution Performance of Ternary $TiO_2/MgTiO_3/C$ Photocatalysts

Zhongmei Yang,[1,3] Yunhong Jiang,[1,3] Wei Zhang,[1] Yanhuai Ding,[1,4,*] Yong Jiang,[1] Jiuren Yin,[1] Ping Zhang,[1,2,*] and Hean Luo[2]

SUMMARY

Solar-driven photochemical hydrogen evolution is a promising route to sustainable hydrogen fuel production. Large-scale preparation of highly active photocatalysts using elementally abundant and less-expensive materials is urgently required for widespread practical application. Here, we report a highly efficient and low-cost $TiO_2/MgTiO_3/C$ heterostructure photocatalyst for photochemical water splitting, which was synthesized on gram scale via a facile mechanochemical method. The heterostructure and carbon sensitization offer excellent photoconversion efficiency as well as good photostability. Under irradiation of one AM 1.5G sunlight, the optimal $TiO_2/MgTiO_3/C$ photocatalyst can show a great solar-driven hydrogen evolution rate (33.3 mmol·h^{-1}·g^{-1}), which is much higher than the best yields ever reported for $MgTiO_3$-related photocatalysts or pure TiO_2 (P-25). We hope this work will attract more attention to inspire further work by others for the development of low-cost, efficient, and robust photocatalysts for producing hydrogen in artificial photosynthetic systems.

INTRODUCTION

Hydrogen is an ecofriendly and renewable energy resource that has been widely investigated to replace traditional fossil fuels because of its high gravimetric energy density. Photocatalytic water splitting under irradiation by solar light has received intense attention for the production of renewable hydrogen from water on a large scale. Great efforts have been devoted to explore effective strategies to design advanced photocatalytic materials (Tong et al., 2012), with rapid progress achieved since the first proposal of water splitting by Honda and Fujishima using a TiO_2 electrode in the early 1970s (Fujishima and Honda, 1972). Photocatalysts play a crucial role for solar-to-hydrogen efficiency by lowering the energetic barriers for reaction as they determine how much photoexcitation occurs in a semiconductor under solar illumination and how many photoexcited carriers reach the surface where water splitting takes place (Hisatomi et al., 2014). Most available water splitting photocatalysts are built using expensive noble metals (such as Pt, Ta, Ru, Ir, and Rh), but for widespread practical applications of photocatalytic hydrogen evolution, one should not only take into account high activity for the photocatalysts but also consider the yield, cost, and environment friendliness. Although new photocatalyst materials for water splitting have recently been developed one after another, very few meet the above requirements, with alternative strategies for the synthesis of cost-effective and highly efficient photocatalytic materials and water splitting still very desirable.

Titanium dioxide (TiO_2) is a promising substrate for the photogeneration of hydrogen from water because of its fascinating features such as chemical inertness, photostability, environment liness, and low cost (Schneider et al., 2014). Numerous groups have worked on the optimization and engineering of TiO_2-based nanostructures, such as elemental doping, forming hybrid architectures, hydrogenization, and constructing heterostructures including wet-chemical and thermochemical approaches (Chen and Burda, 2008; Chen et al., 2011; Lu et al., 2010). Among these approaches, forming a heterojunction with metals or semiconductors has been demonstrated to promote charge separation and transfer of photogenerated electron and hole pairs, and, consequently, improve photocatalytic H_2 generation efficiency (Wang et al., 2014).

Magnesium titanate ($MgTiO_3$), as a member of the perovskite family (such as $SrTiO_3$, $BaTiO_3$, and $CaTiO_3$), has been investigated and employed as a ceramic capacitor and resonator because of its low dielectric loss

[1]Institute of Rheological Mechanics, Xiangtan University, Xiangtan, Hunan 411105, P. R. China

[2]National Engineering Center of Chemical Engineering Process Simulation and Enhancement, Xiangtan University, Xiangtan, Hunan 411105, P. R. China

[3]These authors contributed equally

[4]Lead Contact

*Correspondence: yhding@xtu.edu.cn (Y.D.), zhangp@xtu.edu.cn (P.Z.)

https://doi.org/10.1016/j.isci.2019.03.009

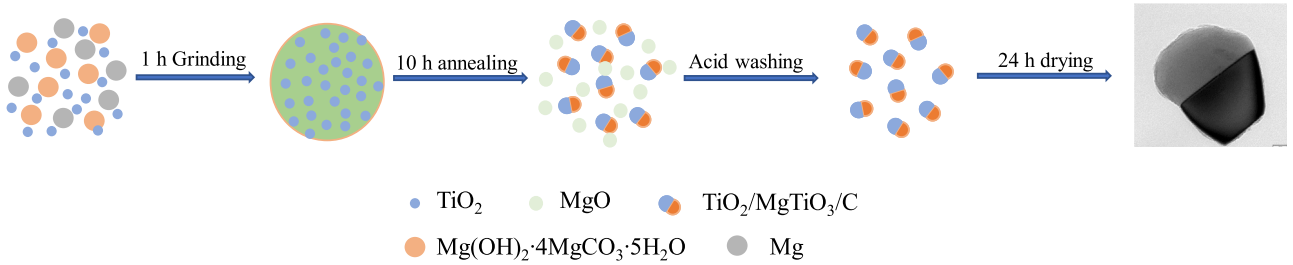

Scheme 1. Schematic Diagram of the Preparation Process of the $TiO_2/MgTiO_3/C$ (TMCs) Samples

The corresponding HRTEM image can be seen in Figure S1.

and high thermal stability at high frequencies (Surendran et al., 2008). Owing to the wide band gap of $MgTiO_3$ (3.5 eV), few scientific groups have studied it as a noble photocatalyst. However, based on the previously reported strategy for photocatalytic water splitting, photocatalysts must have suitable energy levels for the conduction band (CB) and valence band (VB), as the bottom of the CB must be located at a more negative potential than the reduction potential of H^+/H_2 (0 V versus normal hydrogen electrode [NHE]), whereas the top of the VB must exceed the oxidation potential of H_2O to O_2 (1.23 V versus NHE) (Tachibana et al., 2012). $MgTiO_3$ possesses suitable electronic structures and CB (−1.13 eV) or VB (2.37 eV) positions (Zhang et al., 2016b), which matches well with the redox potential of water into hydrogen and oxygen. Moreover, the bottom of the CB of perovskite photocatalysts mainly consists of empty transition-metal *d* orbitals (Ti^{4+}) and is located at a potential more negative than 0 V, which has the potential activity for water splitting (Zhang et al., 2016a). Therefore, due to the good flat-band potential and photovoltage, $MgTiO_3$ may lead itself to be a desirable photocatalyst for water splitting.

Nevertheless, both TiO_2 and $MgTiO_3$ are wide-band-gap semiconductors, which cover only a small fraction (<4%) of the total solar spectrum reaching the surface of the earth. In response to this issue, it is necessary to extend the absorbance spectrum into the visible light region (≈43%). Carbon materials have rapidly emerged due to the unique properties of conjugated materials for electron transport and photoelectronic coupling ability (Yang et al., 2017). In addition, carbon coating offers the intrinsic properties of being stable, inexpensive, able to cover a broader spectrum range, and environment friendly. Herein, we propose that carbon coating should be an ideal candidate for improving the transport of photocarriers through the formation of electronic interactions with $TiO_2/MgTiO_3$ heterostructures. Although the synthesis of carbon-coated photocatalysts and a subsequently enhanced photocatalytic activity have been reported extensively in the literature, the *in situ* formation of a uniform carbon layer onto the surface of a photocatalyst by ingeniously using nascent carbon atoms has never been reported before. The nascent carbon atoms were produced from the reduction of CO_2 by Mg in the calcination process, leading to the formation of the carbon coating.

Synthesis of $MgTiO_3$-related photocatalysts such as $MgTiO_3/MgTi_2O_5/TiO_2$ (Meng et al., 2017), $Si/MgTiO_3$ (Zhu et al., 2016), pure $MgTiO_3$ nanofibers (Wang et al., 2017), and $MgTiO_3/MgTi_2O_5$ (Qu et al., 2013) has been reported by very few groups, but the photocatalytic efficiency is barely satisfactory. In addition, most of the methods are taken in aqueous solution, and they commonly involve organic solvents and produce hazardous by-products, and furthermore, in most cases, the reaction process is difficult to control and shows a low yield (Yang et al., 2018). If the full potential of the materials is to be realized, it is, thus, highly desirable to devise a large-scale and ecofriendly route with reproducible shape control. In response to this important technological challenge, we propose here a facile solid-state reaction as a means of synthesizing carbon-layer-coated $TiO_2/MgTiO_3$ heterostructures in a $Mg(OH)_2·4MgCO_3·5H_2O$ medium at 550°C in the presence of TiO_2 and metal Mg, with the as-prepared photocatalysts showing a robust solar light-driven hydrogen evolution performance.

RESULTS AND DISCUSSION

Scheme 1 is the schematic diagram of the preparation process of the $TiO_2/MgTiO_3/C$ (TMC) samples. In a typical process, nonstoichiometric TiO_2, $Mg(OH)_2·4MgCO_3·5H_2O$, and Mg powder (99.9%) were mixed and ground for 1 h; set weight ratios of 9:1, 7:3, 5:5, and 3:7 for $TiO_2/MgTiO_3$ in TMCs were used for the photocatalyst samples, which were labeled as TMC1, TMC2, TMC3, and TMC4, respectively (Table S1).

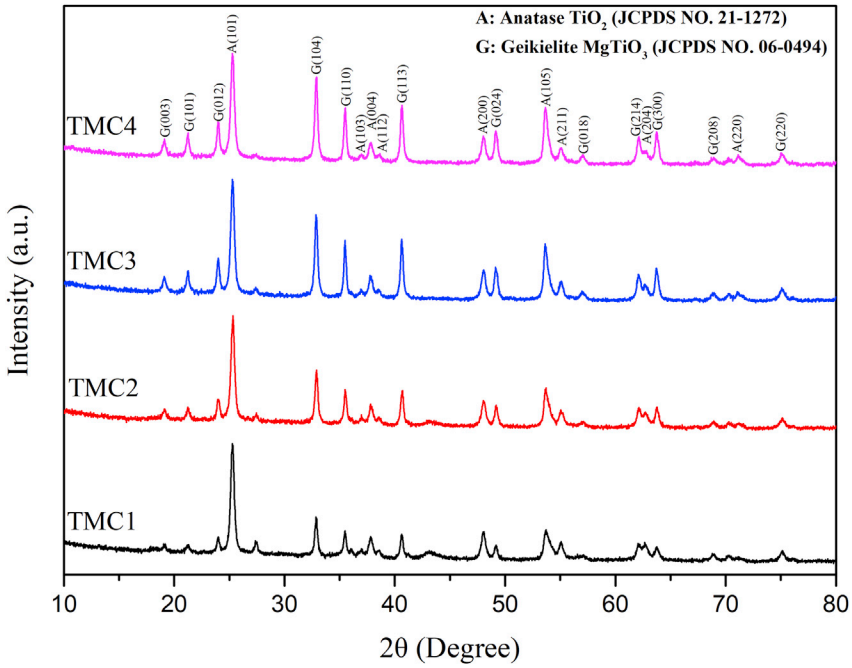

Figure 1. XRD Patterns of TiO_2/$MgTiO_3$/C Samples (TMCs)

The atomic ratios of TMC1, TMC2, TMC3, and TMC4 are 9:1, 4:1, 3:1, and 10:7, respectively. Two sets of diffraction peaks labeled A and G belong to anatase TiO_2 and geikielite $MgTiO_3$, respectively.

The obtained samples contain different Ti/Mg atomic ratios, which could be accurately controlled by adjusting the dosage of precursors according to the chemical reaction equation; then the samples were placed in a corundum crucible and inserted into a tubular furnace, annealed at 550°C under Ar atmosphere for 10 h, and subsequently cooled to room temperature. The mixtures were collected, washed several times with 0.1 mol/L HCl solution and ultrapure water, and then vacuum dried at 70°C overnight in a drying oven. We can easily and routinely scale-up this process to produce grams of TMC heterostructure nanomaterials. All feedstocks were made from elementally abundant and less-expensive materials, with the whole synthetic process not involving the use of any organic solvents and hazardous by-products.

Owing to the heterojunctions, suitable CB/VB positions, and uniform carbon coating, the obtained catalysts exhibited a current density of 0.14 $mA \cdot cm^{-2}$ without a bias voltage, as well as excellent durability. Consequently, under irradiation by simulated sunlight (power: one sunlight), the TMC2 photocatalyst with a Ti/Mg molar ratio of 4:1 can give a great solar-driven hydrogen evolution rate (33.3 $mmol \cdot h^{-1} \cdot g^{-1}$), which is much higher than the best yields ever reported for $MgTiO_3$-related photocatalysts or P-25 TiO_2 (Bin Adnan et al., 2018). The evolution of abundant bubbles, which commenced as soon as the sample was irradiated by either artificial or natural sunlight, can be clearly seen in Videos S1 and S2 (See Supplemental Information for details).

The purity and crystallinity of TMC samples were examined by using powder X-ray diffraction (XRD) (Figure 1). Very few, if any, impurity peaks are present. The XRD patterns clearly show mixed diffraction peaks, which can be indexed to the anatase TiO_2 (JCPDS card No. 21–1272) and geikielite $MgTiO_3$ (JCPDS card No. 06–0494), indicating that $MgTiO_3$ with a high degree of crystallinity was successfully synthesized by our method. With an increasing amount of Mg source, the intensity of the $MgTiO_3$ peaks relatively improved, suggesting a different content of $MgTiO_3$ in the TMC samples. The calculated lattice constants for TiO_2 and $MgTiO_3$ are in good agreement with standard data, and the variation can be ignored, suggesting that elemental doping does not exist in TMC heterostructure materials (Table S2). Carbon-related peaks were not observed because of the low crystallinity.

To reveal the structure, composition, and surface uniformity of the carbon shell, TMC2 was observed using transmission electron microscopy (TEM) and scanning TEM. Figure 2A presents a low-magnification TEM

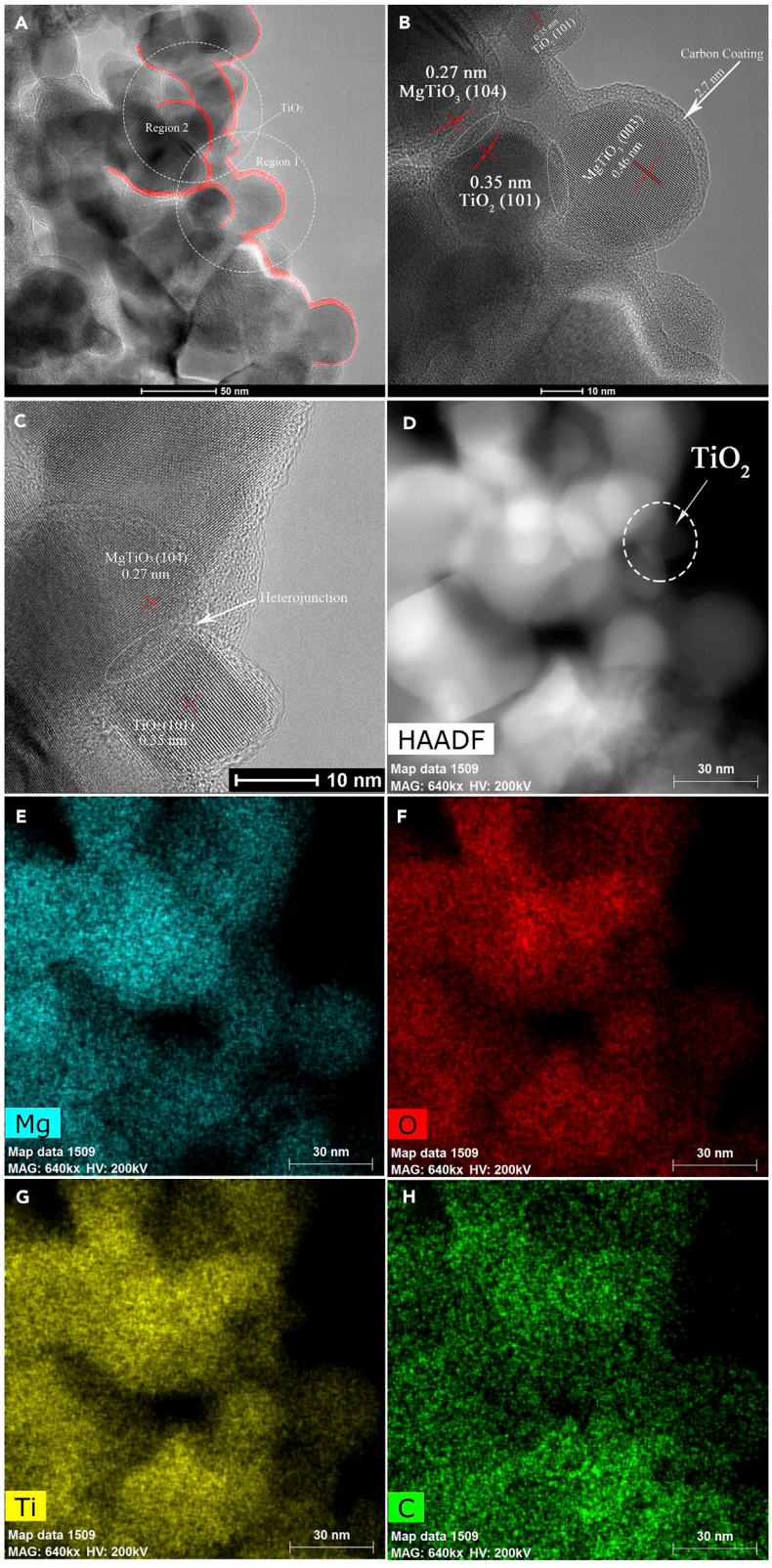
A
Region 2
Region 1
50 nm
B
0.27 nm
MgTiO3 (104)
0.35 nm
TiO2 (101)
Carbon Coating
2.7 nm
10 nm
C
MgTiO3 (104)
0.27 nm
Heterojunction
10 nm
D
TiO2
HAADF
Map data 1509
MAG: 640kx HV: 200kV
30 nm
E
Mg
Map data 1509
MAG: 640kx HV: 200kV
30 nm
F
O
Map data 1509
MAG: 640kx HV: 200kV
30 nm
G
Ti
Map data 1509
MAG: 640kx HV: 200kV
30 nm
H
C
Map data 1509
MAG: 640kx HV: 200kV
30 nm

Figure 2. Structural and Elemental Characterization of TMC2

(A–H) (A) TEM image of TMC2 showing a uniform carbon coating painted in red; (B) HRTEM image of TMC2 from the region 1 in Figure 2A, confirming the phase of TiO_2, $MgTiO_3$, and carbon coating; (C) HRTEM image of TMC2 from the region 2 in Figure 2A, confirming the heterojunction between TiO_2 and $MgTiO_3$; (D) the corresponding high-angle annular dark-field (HAADF) image of Figure 2B. Top-view TEM-EDX elemental mapping images showing a TEM image (A), Mg distribution (E), O distribution (F), Ti distribution (G), and C distribution (H).

image of TMC2, demonstrating a clear amorphous shell on the surface of $TiO_2/MgTiO_3$ nanocomposites (painted as red). Figure 2B shows the high-resolution TEM (HRTEM) image of TMC2 from the region 1 in Figure 2A, which identified a high-quality polycrystalline feature for TMC2 with an amorphous coating layer. Obviously, three sets of lattice fringes were measured with a lattice spacing of 0.46, 0.27, and 0.35 nm, matching well with the (003) and (104) planes of geikielite $MgTiO_3$ and (101) planes of anatase TiO_2, respectively. As shown in Figure 2A, the continuous lattice fringes can be clearly observed at the interfaces (ellipse regions) between TiO_2 and $MgTiO_3$, indicating the formation of heterostructure. In addition, a uniform amorphous coating with a thickness of $\approx$2.7 nm could be clearly observed, which should be the carbon coating. Figure 2C is the HRTEM image of the region 2 in Figure 2A, in which the lattice spacing of the particle next to TiO_2 is 0.27 nm, matching with the (104) planes of geikielite $MgTiO_3$. In Figure 2C, an obvious heterojunction structure can be also found at the interface of the two phases. Figure 2D is the corresponding high-angle annular dark-field image for TMC2 sample taken from the area shown in Figure 2B, which also demonstrates a typical heterostructure nanocomposite based on the different atomic weight. Corresponding elemental mappings (Figures 2E–2H) display the spatial arrangements for the Mg, O, Ti, and C elements in the region, confirming the elemental composition of TMC2. Obviously, C elements exhibited a fairly uniform distribution across the entire nanocomposite, suggesting a carbon shell structure. Note, no Mg signal could be observed in the selective area (circular region) of Figure 2D, indicating that the nanoparticle should be TiO_2, which is consistent with the HRTEM result.

X-ray photoelectron spectroscopy (XPS) was performed to clarify the elemental composition and valence states for the TMC sample (Figure S2). The full scan spectrum in Figure S2A confirms that Mg, Ti, O, and C coexist in the sample, in good accordance with the result from TEM-energy-dispersive X-ray spectroscopy (EDX) elemental mapping. The fine XPS spectrum for the C 1s signal (Figure S2B) was well fitted with three contributions, which could be ascribed to C_n (284.6 eV), C-OH (285.6 eV), and C=O (288.4 eV), respectively. No Ti-C bond (281 eV) was observed, suggesting that the carbon element did not dope into the TMC phase. If the carbon element has a doping state, its content must be extremely low. The nature of the carbon existing in TMC2 was also characterized by Raman spectroscopy, with the result shown in Figure S3 confirming the presence of sp^2 planar and conjugated structures within the carbon layer of TMC2. As shown in Figure S2C, the binding energy between Ti $2p_{1/2}$ (458.5 eV) and Ti $2p_{3/2}$ (464.2 eV) is 5.7 eV, which illustrates a normal state of Ti^{4+} in the sample (Qin et al., 2017). With respect to the high-resolution XPS spectra for O 1s in Figure S2D, the three peaks at 529.7, 530.3, and 531.6 eV were fitted, which should be regarded as Ti-O-Ti (lattice O), Mg-O, and C=O (and COO) species, respectively. The high-resolution XPS spectra for the Mg 1s and Mg 2s are located at 1,304.3 and 89.2 eV (Figures S2E and S2F), respectively, indicating the presence of Mg^{2+} (Zhang et al., 2016b). The XPS results, especially the high-resolution XPS spectra for Mg and Ti, suggest that $MgTiO_3$ formed with Mg and Ti in valences of +2 and +4, respectively. The XRD, TEM, and XPS results confirmed the composition of TiO_2, $MgTiO_3$, and carbon. It should be stressed that the formation of $MgTiO_3$ is due to the calcination process, which was confirmed by the XRD results before heat treatment (Figure S4). After $Mg(OH)_2{\cdot}4MgCO_3{\cdot}5H_2O$ was thermally decomposed to MgO and CO_2, the products continue to react with TiO_2 and Mg to produce $MgTiO_3$ and carbon, respectively. In the post-calcination process, TiO_2 and $MgTiO_3$ form heterojunctions and carbon deposits on their surfaces. As the sintering temperature is kept at 550°C, the reaction between $MgTiO_3$ and TiO_2 will not continue to produce $MgTi_2O_5$, which requires a reaction temperature of more than 1,000°C (Suzuki and Shinoda, 2011). This two-step reaction has been confirmed by the XRD results (Figure 1).

UV-visible diffuse reflectance spectroscopy was employed to characterize the optical properties of TMC serial samples (Figure S5). All samples exhibit enhanced absorption bands from 400 to 800 nm due to the effective light absorption property of the functional carbon coating in TMC nanocomposites. The absorbance was enhanced in sequence from TMC1 to TMC4 with the increase in carbon content. The carbon layer can introduce a sensitization effect to extend the response of $TiO_2/MgTiO_3$ heterostructure materials into the visible light range of the solar spectrum. Moreover, a joint electronic state will form at the interface of a $TiO_2/MgTiO_3$ core and carbon shell, resulting in a synergistic effect (Sahare et al., 2017).

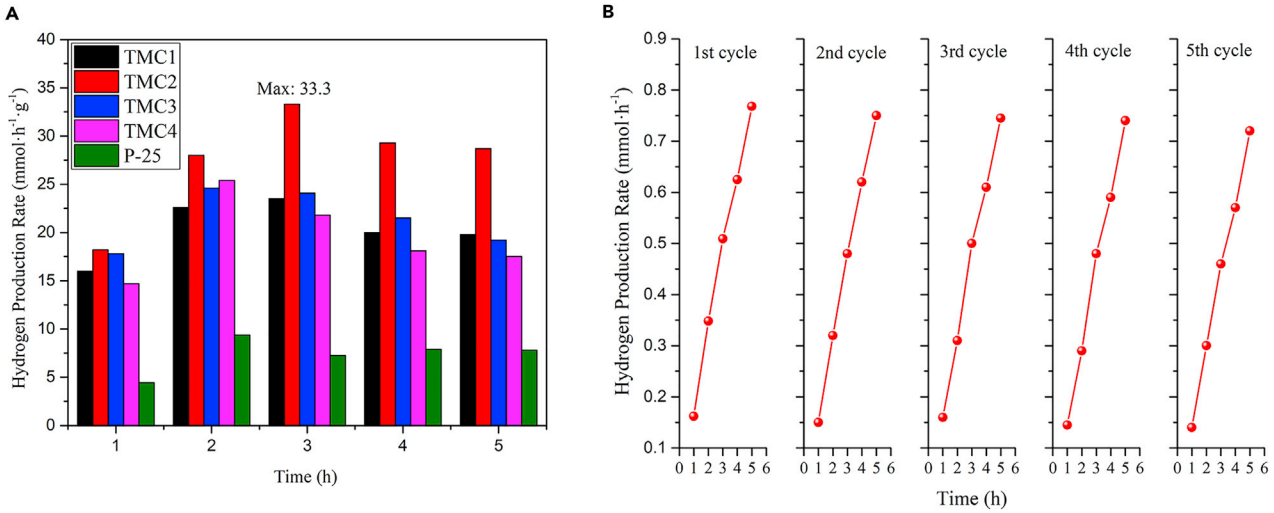

Figure 3. Results of Performance and Optical Stablity Test

(A) Photocatalytic H_2 production curves for TiO_2/$MgTiO_3$/C samples and P-25 TiO_2.

(B) Repeated, photocatalytic water splitting experiments for a TMC2 photocatalyst under AM 1.5 G irradiation.

However, a carbon coating is a double-edged sword: the excessive thickness of a carbon shell will block the absorption of light and decrease the photocatalytic activity to a large extent. In the present work, TMC2 with a carbon coating of 2.7 nm exhibits the best photocatalytic performance, which is consistent with previous reported results, i.e., the optimal thickness for the carbon coating is 1–3 nm (Zhang et al., 2008). In Figure S6, the carbon thickness of TMC1, TMC3, and TMC4 samples was characterized by HRTEM, which was about 1.0, 5.0, and 10 nm, respectively. The thickness of carbon coating is determined by Mg (reductant), $Mg(OH)_2{\cdot}4MgCO_3{\cdot}5H_2O$ (carbon source), and the sintering time; it is reasonable that the thickness of carbon coating increases correspondingly with the increasing mass percentage of $MgTiO_3$. In addition, unlike the general carbon layer produced from carbonization of organic species, here, the carbon layer was formed by reducing CO_2 gas, so it did not contain organic functional groups, which are derived from incomplete graphitization. These functional groups have been demonstrated to be the recombination center for e^-/h^+ pairs, leading to a decrease in the photocatalytic property (Jing et al., 2013).

The time evolution for H_2 production due to solar-driven water splitting with 0.005 g of TMCs and P-25 TiO_2 from a continuous measurement is shown in Figure 3A. The efficiency of the first 2 hours was to be affected by the photodeposition of platinum ions, and then reached peak value at the third hour; the slight decline in performance at the last 2 hours is due to the adverse reaction caused by the generated hydrogen in the test system, or the consumption of sacrificial agents. Different molar ratios for Ti/Mg give different H_2 production efficiencies; when the atomic ratio of Ti/Mg ≈ 4:1, one reaches the best photocatalytic performance. The rate of hydrogen production is 33.3 $mmol{\cdot}h^{-1}{\cdot}g^{-1}$, which is much higher than the best yield ever reported for $MgTiO_3$-related photocatalysts or pure TiO_2 (Degussa P-25, 7.9 $mmol{\cdot}h^{-1}{\cdot}g^{-1}$) (Bin Adnan et al., 2018). Besides, it is necessary to compare TMCs with the recent achievements of TiO_2-based materials for photocatalytic H_2 production. Based on the reported works, such as $SrSO_4/TiO_2/Pt$ (10.5 $mmol{\cdot}h^{-1}{\cdot}g^{-1}$) (Wang et al., 2019), Pt^0 and oxidized Pt^{2+}-modified TiO_2 nanosheets (20.88 $mmol{\cdot}h^{-1}{\cdot}g^{-1}$) (Jin et al., 2017), Bi_2O_3@TiO_2 nanotubes (26.02 $mmol{\cdot}h^{-1}{\cdot}g^{-1}$) (Lakshmana Reddy et al., 2017), Cu(II) pre-grafted Pt/TiO_2 (27.2 $mmol{\cdot}h^{-1}{\cdot}g^{-1}$) (Dozzi et al., 2017), C/TiO_2 nanotube/carbon nanotubes (37.6 $mmol{\cdot}h^{-1}{\cdot}g^{-1}$) (Zhao et al., 2014), and Mg-reduced black TiO_2 (43 $mmol{\cdot}h^{-1}{\cdot}g^{-1}$) (Sinhamahapatra et al., 2015), whether or not the photocatalytic hydrogen production rate of TMC samples is the highest, considering the simplicity, environment friendliness, low-cost, and high yield of the synthesis method, TMC photocatalysts still have great advantages. Figure 3B shows repeated, photocatalytic water splitting experiments for the TMC2 photocatalyst under AM 1.5 G illumination, which exhibits a good durability without a significant drop in activity; even after the fifth cycle (25 h), the hydrogen production efficiency loss is less than 5%. The XRD analysis of TMC2 sample after 25 h of photochemical reaction shows that the compositions and crystal structures of TMC2 do not change (Figure S7). This confirms our previous

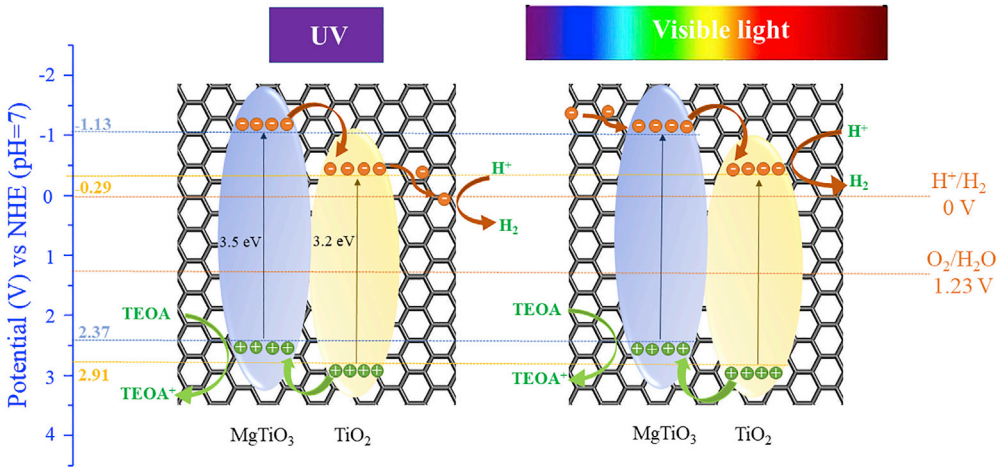

Scheme 2. Schematic Illustration for the Charge Separation and Transfer Over the $TiO_2/MgTiO_3$/C Nanocomposites under Different Spectrum Regions

assumption that slight performance degradation is due to the consumption of sacrificial agents or the adverse reaction. The photostability result suggests that TMC2 heterostructure materials are promising stable photocatalysts under solar light, which should result from the protection afforded by the uniform carbon coating (Wang et al., 2016).

Scheme 2 depicts the charge separation and transfer over the TMC nanocomposite, which has two different situations in UV and visible light regions. In the UV region, $MgTiO_3$ is excited by the high-energy UV light to produce photogenerated electron-hole pairs. Driven by the internal electric field of the heterojunction, photogenerated electrons are transferred to the CB of TiO_2, whereas holes are transferred in the opposite direction, which makes them difficult to recombine. In addition, carbon is a kind of high-work-function material, so the photogenerated electrons are quickly transferred to the reaction sites because of the electrostatic attraction, where carbon coating can trap electrons due to its good conductivity (Pan et al., 2017). Thus the possibility for recombination of e^-/h^+ pairs decreases.

Based on the reported works, carbon coating will couple with the undercoordinated Ti atoms to restructure into an optimal structure (Lee et al., 2012); this kind of hybrid effect in TMCs plays an important role in visible light region. Figure 4A shows the hydrogen production performance of TMC2 and P-25 TiO_2 under irradiation of AM 1.5G or pure visible light. The TMC2 sample could still maintain a hydrogen production efficiency of 1.46 $mmol \cdot h^{-1} \cdot g^{-1}$ after switching the light source to pure visible light. As comparison, hydrogen production cannot be observed when P-25 TiO_2 was used. This result suggests that TMC2 enhances the absorption and utilization of visible light. First, carbon coating is excited by visible light to produce excited state electrons, and then the electrons are injected to the CB of $MgTiO_3$ by the *d*-π conjugation. Owing to the electric field in the heterojunction, the electrons will continue to transfer to the CB of TiO_2 and follow to react with water on the surface. Therefore, the carbon shell enables TMC samples to absorb a high amount of photoenergy in the visible region, effectively driving the photochemical hydrogen evolution reaction.

To understand the correlation between the photoactivity and light absorption, the incident photon to charge carrier generation efficiency (IPCE) of P-25 TiO_2 and TMC2 photoanodes were measured at 0.23 V versus Ag/AgCl. The IPCE was calculated according to the following equation (Shi et al., 2018):

$$\mathrm{IPCE}(\%) = \frac{1240 \times I_{sc}(mA \cdot cm^{-2})}{\lambda(\mathrm{nm}) \times I_{inc}(mW \cdot cm^{-2})} \times 100$$

where I_{sc} is the photocurrent density ($mA \cdot cm^{-2}$) under illumination, λ is the wavelength (nm) of incident radiation, and I_{inc} is the incident light power intensity on the TMC2 electrode ($mW \cdot cm^{-2}$). Compared with P-25 TiO_2, the photoactivity of TMC2 sample in the UV region was significantly enhanced and the IPCE value in the wavelength range from 300 to 370 nm was close to 90% (Figure 4B). It illustrates that the separation and transport efficiency of photoinduced carriers of TMC2 sample under UV irradiation is greatly

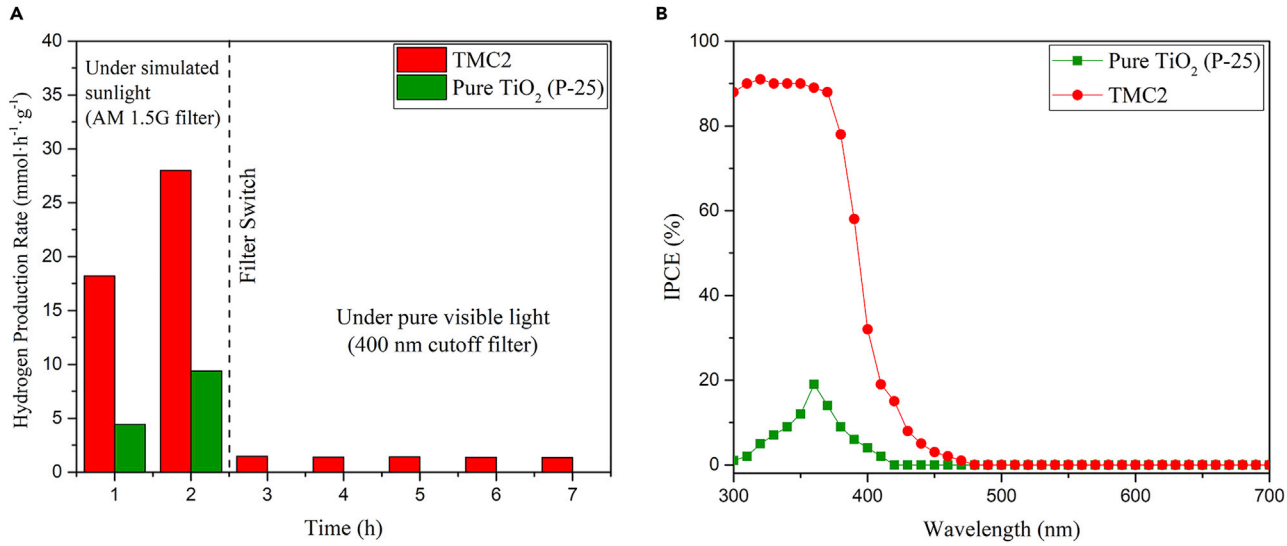

Figure 4. Performance Test and IPCE Spectra of P-25 TiO_2 and TMC2

(A) Photocatalytic H_2 production curves for TMC2 sample and P-25 TiO_2 under simulated sunlight or pure visible light.

(B) IPCE spectra in the wavelength of 300–700 nm at 0.23 V versus Ag/AgCl.

improved. In addition, we found that the IPCE value of TMC2 is higher than that of P-25 TiO_2 in the visible light region from 400 to 470 nm, which means that TMC2 sample not only has good UV photoelectric conversion efficiency but also can absorb and utilize an amount of visible light.

To evaluate the photocatalytic water splitting activity of TMCs and further illustrate the enhanced electron transfer in samples, the photoelectrochemical properties of TMCs were investigated. Figure 5A shows plots for the transient photocurrent response (TPC) versus time for TMCs without bias voltage, which was carried out under AM 1.5G illumination with several 30-s light on/off cycles. All the four samples show a good photoresponse for chopped-light cycles. The photocurrent values are almost zero without light source, whereas the photocurrent rapidly restores to a steady-state value upon irradiation, which is reproducible for several on/off cycles with almost identical photocurrent and dark current (the evolution of abundant bubbles commenced as soon as the sample was irradiated by light and stopped after the light was cut off, which can be clearly seen in Video S3). TMC2 shows the best steady-state photocurrent (0.14 $mA \cdot cm^{-2}$), indicating that a large number of photoinduced carriers are present in TMC2 due to the improved charge separation and a more efficient transfer process from $TiO_2/MgTiO_3$ heterojunctions to the carbon shell. Figure 5B shows a set of linear sweeps recorded under AM 1.5 G illumination. The potential was swept linearly at a scan rate of 0.1 V/s between −2.0 and 2.0 V versus Ag/AgCl in 0.5 M Na_2SO_4 electrolyte (pH = 6.82). Obviously, the photocurrent for TMC2 is distinctly higher than that of the other samples, indicating more efficient separation of the photogenerated e^-/h^+ pairs in TMC2 at the interfaces, which enables more charge carriers to form reactive species, thereby generating a higher photocurrent response. Moreover, the onset potential for the photocurrent reveals a slight shift from −1.35 V for TMC1 to −1.50 V for TMC2. The higher photocurrent density and lower onset potential indicates more efficient charge separation and transport in the TMC2 (Cui et al., 2014). This result should be attributed to the enhanced visible-light absorption of TMCs that is mainly caused by the photosensitization of the carbon coating, which contributes to the overall photocatalytic performance. The measurement of electrochemical impedance can provide further evidence of carrier separation efficiency in the as-prepared TMC samples. The radius of the semicircle on the electrochemical impedance spectra (EIS) reflects the interface layer resistance at the electrode surface. The smaller arc radius implies higher efficiency for charge transfer (Liu et al., 2016). The Nyquist plots showing the EIS in Figure 5C show that the interfacial resistance for TMC2 is much smaller than the other samples, indicating that charge separation in TMC2 is more efficient. Therefore, we can conclude that charge transfer is facilitated across the interfaces between the $TiO_2/MgTiO_3$ heterojunctions and carbon shell. The Mott-Schottky (MT) plots for TMC1 and TMC2 show a positive slope (Figure 5D), characteristic of an n-type semiconductor. The difference in the slopes for the two plots suggests an obvious disparity for the donor

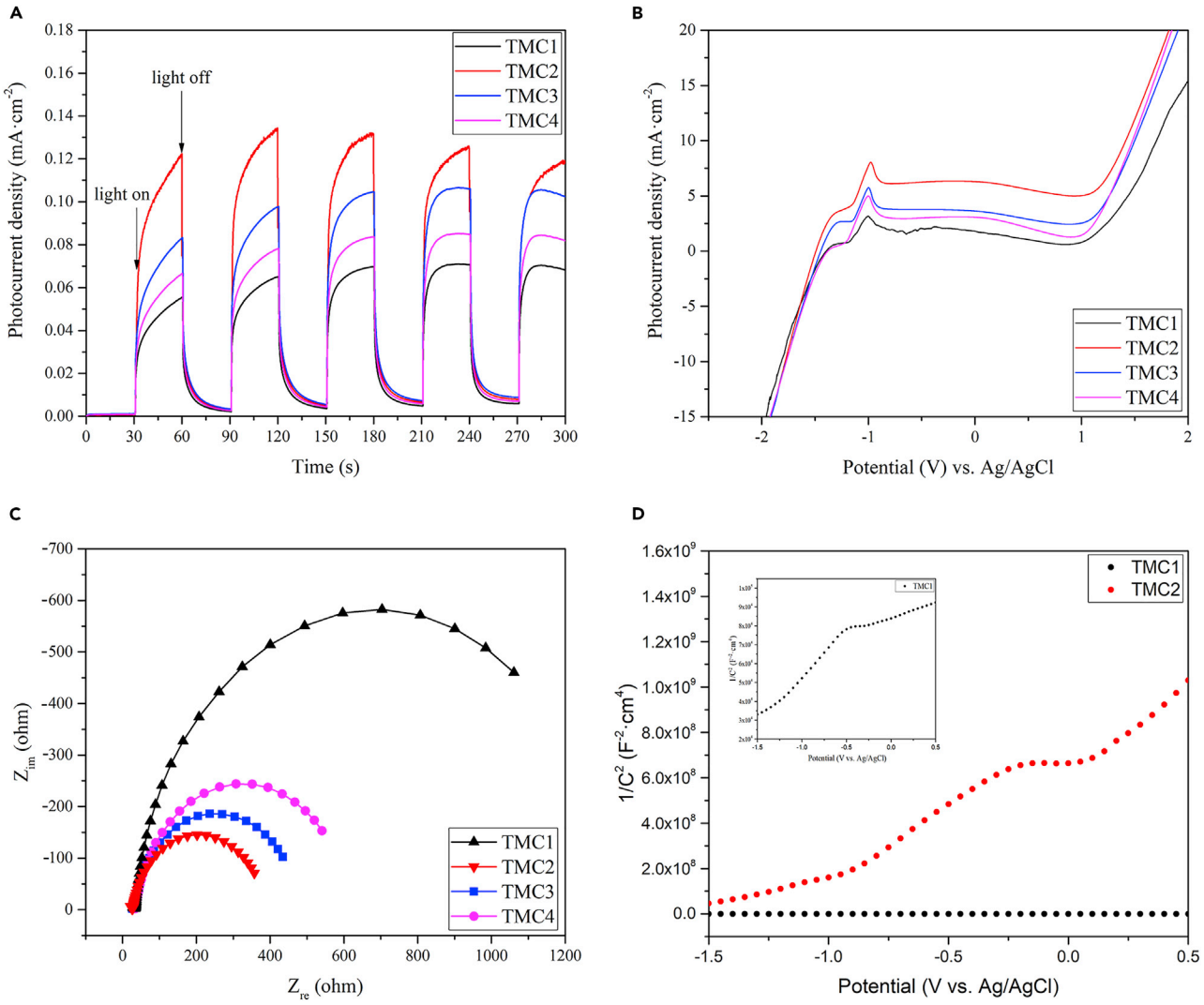

Figure 5. Results of Photoelectrochemical (PEC) Test

(A) Transient photocurrent responses for $TiO_2/MgTiO_3/C$ samples without bias voltage.

(B) Linear-sweep voltammograms collected under 100 mW•cm^{-2} illumination using a three-electrode setup (TMCs working, Pt counter, Ag/AgCl reference electrode, scan rate of 0.1 V/s in 0.5 M Na_2SO_4 electrolyte [pH = 6.82]).

(C) Nyquist plots showing the electrochemical impedance spectra for the TMCs.

(D) Mott-Schottky (MT) plots for TMC1 and TMC2 collected at a frequency of 1 kHz in the dark (the inset image shows a magnified MT plot for TMC1).

densities in TMC1 and TMC2. Carrier density could be calculated from the slope with the following equation:

$$N_d = \left(\frac{2}{e_0 \varepsilon \varepsilon_0}\right)\left[d\left(1/C^2\right)/dV\right]^{-1}$$

where e_0 is the electron charge of 1.602 × 10^{-19} C, ε is the relative permittivity of 31 (for anatase), ε_0 is the vacuum permittivity of 8.854 × 10^{12} F·m^{-1}, N_d is the carrier density, and $d(1/C^2)/dV$ is the straight slope (Song et al., 2018). The calculated electron densities for TMC1 and TMC2 are 4.54 × 10^{19} and 3.85 × 10^{21} cm^{-3}, respectively. The electron density for TMC2 is approximately two orders magnitude higher than that for TMC1. This indicates that the nanostructure in ternary TMC composites produces an exponential increase of the electron density due to the heterojunctions at the interfaces. In addition, the expected upward shift of the Fermi level caused by the appropriate carbon shell can lead to a decrease in bending of the band edge at the surface of TMC2, facilitating charge separation at the interface (Narayan et al., 2014). Therefore, the improved charge transport, along with the facilitated charge separation, is

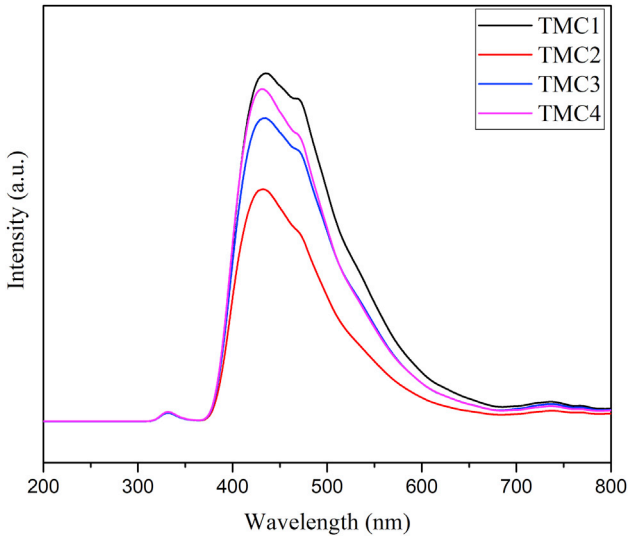

Figure 6. Room Temperature PL Spectra for TiO_2/$MgTiO_3$/C Samples

TMC2 sample (red line) exhibits the lowest emission intensity, suggesting more efficient separation and transfer of the photogenerated e^-/h^+ pairs.

responsible for the much more efficient photochemical water splitting. As discussed above, TPC, linear-sweep voltammograms, EIS, and MT results not only correlate well with each other but also are consistent with the performance-testing results. We believe that better photocatalytic performance for TMCs could be achieved by optimizing the Ti/Mg molar ratio and the thickness of the carbon shell.

A photoluminescence (PL) emission test is usually used to evaluate the efficiency of charge carrier trapping, migration, and transfer in a semiconductor, as lower emission intensity means lower recombination rate for the charge carriers (Li et al., 2013). Figure 6 shows PL spectra for the TMC samples measured using an excitation wavelength of 325 nm at room temperature; all the samples show a band-edge emission peak centered at approximately 430 nm in the visible region, which is caused by the recombination of the photo-induced e^-/h^+ pairs (Wang et al., 2009). As shown in Figure 6, the band-edge emission intensity for TMC1 ~4 is remarkably quenched, indicating the presence of a direct interaction among TiO_2, $MgTiO_3$, and the carbon layer, which enhances the nonradiative relaxation of excitons formed in TMCs. TMC2 exhibits the lowest emission intensity, which means an obvious lower recombination rate, i.e., a more efficient separation and transfer of photogenerated e^-/h^+ pairs, with the lifetime of the charge carriers effectively lengthened. This is in accordance with the photoelectrochemical (PEC) and performance-testing results. Therefore, PL results demonstrate that heterostructures and carbon coating accelerate the separation of e^-/h^+ pairs and inhibit the recombination of direct and trap-related charge carriers because the photoinduced electrons can swiftly transfer to the carbon layer through the heterojunctions, following to react with water to produce hydrogen.

In conclusion, we have synthesized and characterized a stable, robust, and promising material for potential use in photocatalytic hydrogen production. The optimal sample shows a great hydrogen production rate (33.3 $mmol \cdot h^{-1} \cdot g^{-1}$), indicating that TMC heterostructure materials are very effective at separating photo-induced e^-/h^+ pairs and strongly inhibiting their recombination. A deep discussion into the mechanism for improved photocatalytic activity was investigated carefully. We believe this work may open up new insights to develop large-scale, inexpensive photocatalysts with high solar energy conversion efficiency in artificial photosynthetic systems.

METHODS

All methods can be found in the accompanying Transparent Methods supplemental file.

Limitations of the Study

The Ti/Mg molar ratio and the thickness of the carbon shell could be optimized, and the modulation of the exposed facets of the catalyst would be valuable.

SUPPLEMENTAL INFORMATION

Supplemental Information can be found online at https://doi.org/10.1016/j.isci.2019.03.009.

ACKNOWLEDGMENTS

This work was financially supported by the National Natural Science Foundation of China (No. 21376199 and 51002128), Scientific Research Foundation of Hunan Provincial Education Department (No.17A205), Natural Science Foundation of Hunan Province (No. 2018JJ2393), and Postgraduate Innovation Foundation of Hunan Province (No. CX2016B269).

AUTHOR CONTRIBUTIONS

Y.D. and P.Z. designed and conceived this work; Z.Y. and Yunhong Jiang contributed equally to this work and carried out the synthesis, characterization, and the catalytic test. W.Z., Yong Jiang, J.Y., and H.L. analyzed the catalytic results. Z.Y. and Y.D. wrote the paper, and all the authors participated in the discussion of the results.

DECLARATION OF INTERESTS

The authors declare no competing interests.

Received: December 11, 2018
Revised: January 21, 2019
Accepted: March 8, 2019
Published: April 26, 2019

REFERENCES

Bin Adnan, M.A., Arifin, K., Minggu, L.J., and Kassim, M.B. (2018). Titanate-based perovskites for photochemical and photoelectrochemical water splitting applications: a review. Int. J. Hydrogen Energy *43*, 23209–23220.

Chen, X., and Burda, C. (2008). The electronic origin of the visible-light absorption properties of C-, N- and S-doped TiO_2 nanomaterials. J. Am. Chem. Soc. *130*, 5018–5019.

Chen, X., Liu, L., Yu, P.Y., and Mao, S.S. (2011). Increasing solar absorption for photocatalysis with black hydrogenated titanium dioxide nanocrystals. Science *331*, 746–750.

Cui, H., Zhao, W., Yang, C., Yin, H., Lin, T., Shan, Y., Xie, Y., Gu, H., and Huang, F. (2014). Black TiO_2 nanotube arrays for high-efficiency photoelectrochemical water-splitting. J. Mater. Chem. A *2*, 8612–8616.

Dozzi, M.V., Chiarello, G.L., Pedroni, M., Livraghi, S., Giamello, E., and Selli, E. (2017). High photocatalytic hydrogen production on Cu(II) pre-grafted Pt/TiO_2. Appl. Catal. B Environ. *209*, 417–428.

Fujishima, A., and Honda, K. (1972). Electrochemical photolysis of water at a semiconductor electrode. Nature *238*, 37.

Hisatomi, T., Kubota, J., and Domen, K. (2014). Recent advances in semiconductors for photocatalytic and photoelectrochemical water splitting. Chem. Soc. Rev. *43*, 7520–7535.

Jin, J., Wang, C., Ren, X.-N., Huang, S.-Z., Wu, M., Chen, L.-H., Hasan, T., Wang, B.-J., Li, Y., and Su, B.-L. (2017). Anchoring ultrafine metallic and oxidized Pt nanoclusters on yolk-shell TiO_2 for unprecedentedly high photocatalytic hydrogen production. Nano Energy *38*, 118–126.

Jing, L., Zhou, W., Tian, G., and Fu, H. (2013). Surface tuning for oxide-based nanomaterials as efficient photocatalysts. Chem. Soc. Rev. *42*, 9509–9549.

Lakshmana Reddy, N., Emin, S., Valant, M., and Shankar, M.V. (2017). Nanostructured Bi_2O_3@TiO_2 photocatalyst for enhanced hydrogen production. Int. J. Hydrogen Energy *42*, 6627–6636.

Lee, J.S., You, K.H., and Park, C.B. (2012). Highly photoactive, low bandgap TiO_2 nanoparticles wrapped by graphene. Adv. Mater. *24*, 1084–1088.

Li, M., Luo, W., Cao, D., Zhao, X., Li, Z., Yu, T., and Zou, Z. (2013). A co-catalyst-loaded Ta_3N_5 photoanode with a high solar photocurrent for water splitting upon facile removal of the surface layer. Angew. Chem. Int. Ed. *52*, 11016–11020.

Liu, G., Zhao, G., Zhou, W., Liu, Y., Pang, H., Zhang, H., Hao, D., Meng, X., Li, P., Kako, T., et al. (2016). In Situ bond modulation of graphitic carbon nitride to construct p-n homojunctions for enhanced photocatalytic hydrogen production. Adv. Funct. Mater. *26*, 6822–6829.

Lu, X., Huang, F., Mou, X., Wang, Y., and Xu, F. (2010). A general preparation strategy for hybrid TiO_2 hierarchical spheres and their enhanced solar energy utilization efficiency. Adv. Mater. *22*, 3719–3722.

Meng, L., Ren, Z., Zhou, W., Qu, Y., and Wang, G. (2017). $MgTiO_3$/$MgTi_2O_5$/TiO_2 heterogeneous belt-junctions with high photocatalytic hydrogen production activity. Nano Res. *10*, 295–304.

Narayan, M.U., Jun, L.W., Min, L.J., Youngtak, O., Young, K.J., Eun, K.J., Jongwon, S., Hee, H.T., and Ouk, K.S. (2014). 25th anniversary article: chemically modified/doped carbon nanotubes & graphene for optimized nanostructures & nanodevices. Adv. Mater. *26*, 40–67.

Pan, Y.X., You, Y., Xin, S., Li, Y., Fu, G., Cui, Z., Men, Y.L., Cao, F.F., Yu, S.H., and Goodenough, J.B. (2017). Photocatalytic CO_2 reduction by carbon-coated indium-oxide nanobelts. J. Am. Chem. Soc. *139*, 4123–4129.

Qin, N., Xiong, J., Liang, R., Liu, Y., Zhang, S., Li, Y., Li, Z., and Wu, L. (2017). Highly efficient photocatalytic H_2 evolution over MoS_2/CdS-TiO_2 nanofibers prepared by an electrospinning mediated photodeposition method. Appl. Catal. B Environ. *202*, 374–380.

Qu, Y., Zhou, W., Xie, Y., Jiang, L., Wang, J., Tian, G., Ren, Z., Tian, C., and Fu, H. (2013). A novel phase-mixed $MgTiO_3$-$MgTi_2O_5$ heterogeneous nanorod for high efficiency photocatalytic hydrogen production. Chem. Commun. (Camb.) *49*, 8510–8512.

Sahare, S., Ghoderao, P., Dey, A., Datar, S., and Bhave, T. (2017). Study of modification of photo active material with carbon nanostructures for polymer solar cell applications. Mater. Today Commun. *12*, 11–18.

Schneider, J., Matsuoka, M., Takeuchi, M., Zhang, J., Horiuchi, Y., Anpo, M., and Bahnemann, D.W. (2014). Understanding TiO_2 photocatalysis: mechanisms and materials. Chem. Rev. *114*, 9919–9986.

Shi, X., Ueno, K., Oshikiri, T., Sun, Q., Sasaki, K., and Misawa, H. (2018). Enhanced water splitting under modal strong coupling conditions. Nat. Nanotechnol. *13*, 953–958.

Sinhamahapatra, A., Jeon, J.-P., and Yu, J.-S. (2015). A new approach to prepare highly active and stable black titania for visible light-assisted

hydrogen production. Energy Environ. Sci. *8*, 3539–3544.

Song, X., Li, W., He, D., Wu, H., Ke, Z., Jiang, C., Wang, G., and Xiao, X. (2018). The "Midas Touch" transformation of TiO_2 nanowire arrays during visible light photoelectrochemical performance by carbon/nitrogen coimplantation. Adv. Energy Mater. *8*, 1800165.

Surendran, K.P., Wu, A., Vilarinho, P.M., and Ferreira, V.M. (2008). Sol-Gel synthesis of low-loss $MgTiO_3$ thin films by a non-methoxyethanol route. Chem. Mater. *20*, 4260–4267.

Suzuki, Y., and Shinoda, Y. (2011). Magnesium dititanate ($MgTi_2O_5$) with pseudobrookite structure: a review. Sci. Technol. Adv. Mater. *12*, 034301.

Tachibana, Y., Vayssieres, L., and Durrant, J.R. (2012). Artificial photosynthesis for solar water-splitting. Nat. Photonics *6*, 511.

Tong, H., Ouyang, S., Bi, Y., Umezawa, N., Oshikiri, M., and Ye, J. (2012). Nano-photocatalytic materials: possibilities and challenges. Adv. Mater. *24*, 229–251.

Wang, H., Zhang, L., Chen, Z., Hu, J., Li, S., Wang, Z., Liu, J., and Wang, X. (2014). Semiconductor heterojunction photocatalysts: design, construction, and photocatalytic performances. Chem. Soc. Rev. *43*, 5234–5244.

Wang, L., Yang, G., Peng, S., Wang, J., Ji, D., Yan, W., and Ramakrishna, S. (2017). Fabrication of $MgTiO_3$ nanofibers by electrospinning and their photocatalytic water splitting activity. Int. J. Hydrogen Energy *42*, 25882–25890.

Wang, Q., Hisatomi, T., Jia, Q., Tokudome, H., Zhong, M., Wang, C., Pan, Z., Takata, T., Nakabayashi, M., Shibata, N., et al. (2016). Scalable water splitting on particulate photocatalyst sheets with a solar-to-hydrogen energy conversion efficiency exceeding 1%. Nat. Mater. *15*, 611–615.

Wang, X., Maeda, K., Chen, X., Takanabe, K., Domen, K., Hou, Y., Fu, X., and Antonietti, M. (2009). Polymer semiconductors for artificial photosynthesis: hydrogen evolution by mesoporous graphitic carbon nitride with visible light. J. Am. Chem. Soc. *131*, 1680–1681.

Wang, Z., Yang, Q., Liu, W., Ran, H., Zhang, C., Han, X., He, X., Wang, X., and Hu, C. (2019). Optical porous hollow-boxes assembled by $SrSO_4/TiO_2$/Pt nanoparticles for high performance of photocatalytic H_2 evolution. Nano Energy *59*, 129–137.

Yang, G., Wang, L., Zhao, Y., Peng, S., Wang, J., Ji, D., Wang, Z., Yan, W., and Ramakrishna, S. (2018). One-dimensional $Mg_xTi_yO_{x+2y}$ nanostructures: general synthesis and enhanced photocatalytic performance. Appl. Catal. B Environ. *225*, 332–339.

Yang, Z., Jiang, Y., Yu, Q., Ding, Y., Jiang, Y., Yin, J., and Zhang, P. (2017). Facile preparation of exposed {001} facet TiO_2 nanobelts coated by monolayer carbon and its high-performance photocatalytic activity. J. Mater. Sci. *52*, 13586–13595.

Zhang, G., Liu, G., Wang, L., and Irvine, J.T. (2016a). Inorganic perovskite photocatalysts for solar energy utilization. Chem. Soc. Rev. *45*, 5951–5984.

Zhang, L.-W., Fu, H.-B., and Zhu, Y.-F. (2008). Efficient TiO_2 photocatalysts from surface hybridization of TiO_2 particles with graphite-like carbon. Adv. Funct. Mater. *18*, 2180–2189.

Zhang, N., Qu, Y., Pan, K., Wang, G., and Li, Y. (2016b). Synthesis of pure phase $Mg_{1.2}Ti_{1.8}O_5$ and $MgTiO_3$ nanocrystals for photocatalytic hydrogen production. Nano Res. *9*, 726–734.

Zhao, C., Luo, H., Chen, F., Zhang, P., Yi, L., and You, K. (2014). A novel composite of TiO_2 nanotubes with remarkably high efficiency for hydrogen production in solar-driven water splitting. Energy Environ. Sci. *7*, 1700–1707.

Zhu, W., Han, D., Niu, L., Wu, T., and Guan, H. (2016). Z-scheme Si/$MgTiO_3$ porous heterostructures: noble metal and sacrificial agent free photocatalytic hydrogen evolution. Int. J. Hydrogen Energy *41*, 14713–14720.

ISCI, Volume *14*

Supplemental Information

Solid-State, Low-Cost, and Green Synthesis and Robust Photochemical Hydrogen Evolution Performance of Ternary $TiO_2/MgTiO_3/C$ Photocatalysts

Zhongmei Yang, Yunhong Jiang, Wei Zhang, Yanhuai Ding, Yong Jiang, Jiuren Yin, Ping Zhang, and Hean Luo

Supplementary Figures

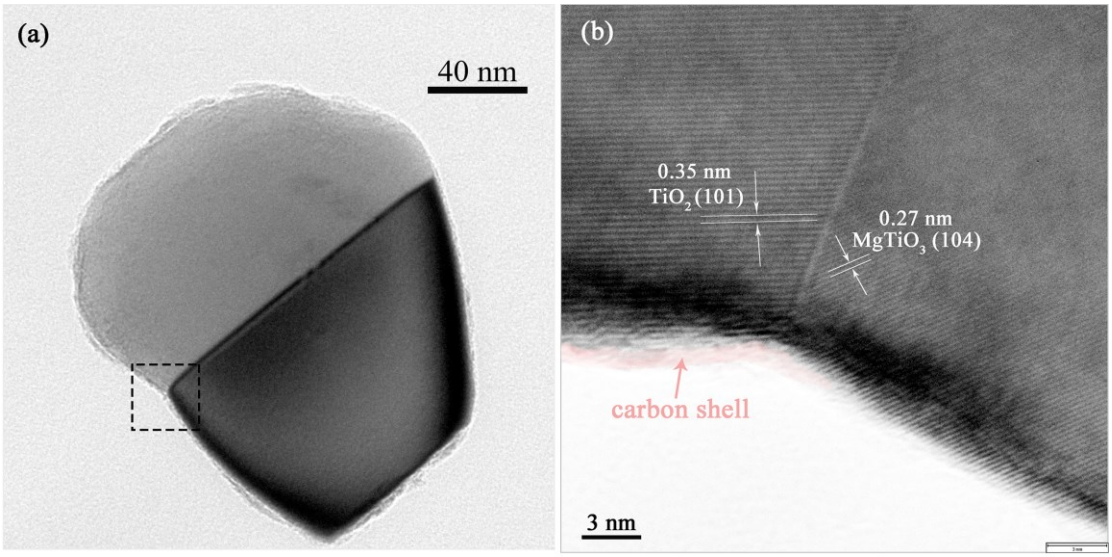

Figure S1. The TEM and HRTEM images of a single $TiO_2/MgTiO_3/C$ nanoparticle, related to **Scheme 1**. (a) The TEM image of a single $TiO_2/MgTiO_3/C$ nanoparticle; (b) The corresponding HRTEM image from the black square frame in Fig. S1a, confirming the phase of TiO_2, $MgTiO_3$ and carbon coating (painted as red). In Fig. S1b, two sets of lattice fringes were measured with a lattice spacing of 0.27 and 0.35 nm, matching well with the (104) and (101) planes of geikielite $MgTiO_3$ and anatase TiO_2, respectively.

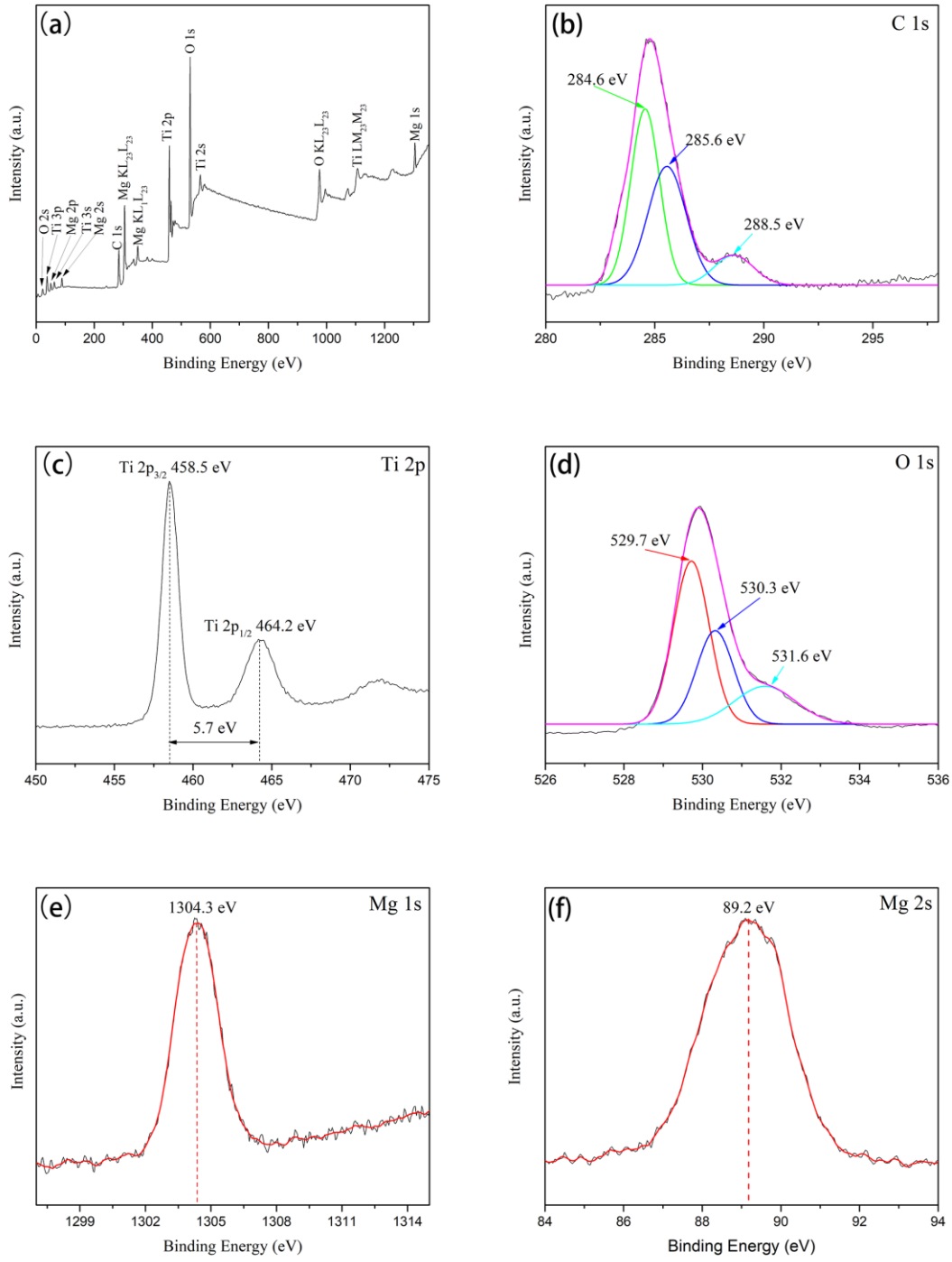

Figure S2. The full and high-resolution XPS spectrums of TMC2, related to **Figure 2.**

(a) The full XPS spectrum. (b) C 1s. (c) Ti 2p. (d) O 1s. (e) Mg 1s. (f) Mg 2s.

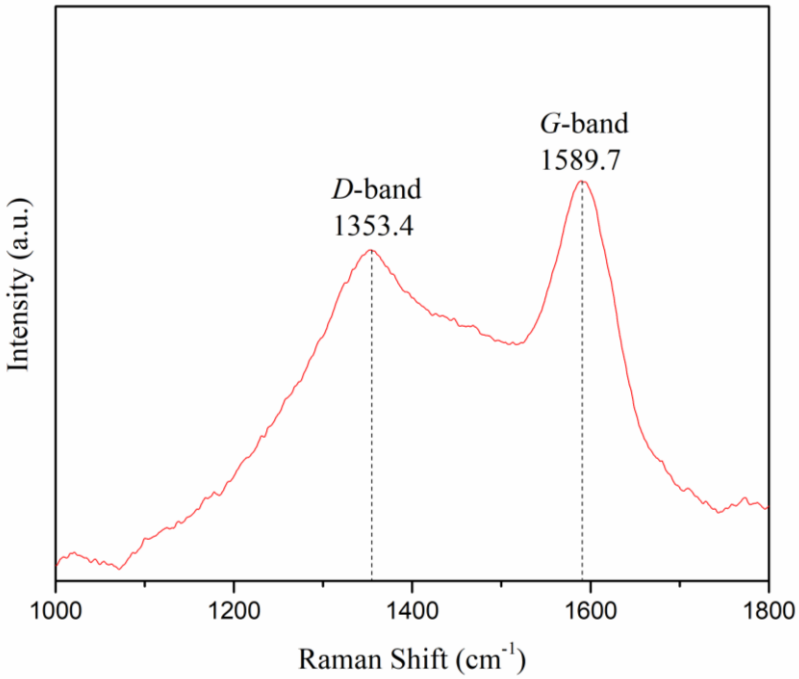

Figure S3. Raman spectra of TMC2, related to **Figure 2.** The two intense broad peaks around at 1353.4 and 1589.7 cm^{-1}, which are respectively assigned to the *D*- and *G*-band of the carbon layer. The Raman-active E_{2g} mode at 1589.7 cm^{-1} is characteristic for graphite-like shell, which confirms the presence of sp^2 planar and conjugated structures within the carbon layer of TMC2. The *D*-band at around 1353.4 cm^{-1} can be attributed to the presence of the disordered graphite-like carbon within the hexagonal structure. The I_D/I_G ratio is indicative of the quality degree of the carbon coating, the relatively low ratio (~ 0.85) means that TMC2 with thinner carbon coating of good contact formed a more ordered carbon structure during the calcination procedure.

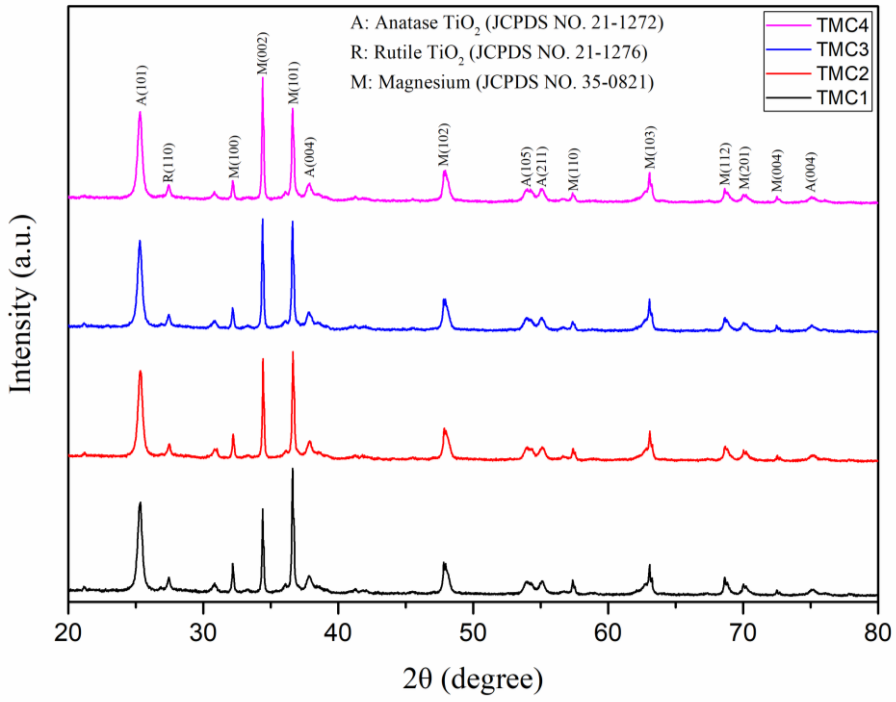

Figure S4. XRD patterns of TiO_2/$MgTiO_3$/C samples before heat treatment, related to **Figure 1**. The diffraction peaks could be ascribed to TiO_2 (Degussa, P-25) and metal Mg, no peaks belong to $MgTiO_3$, indicating that $MgTiO_3$ was not formed yet after grinding.

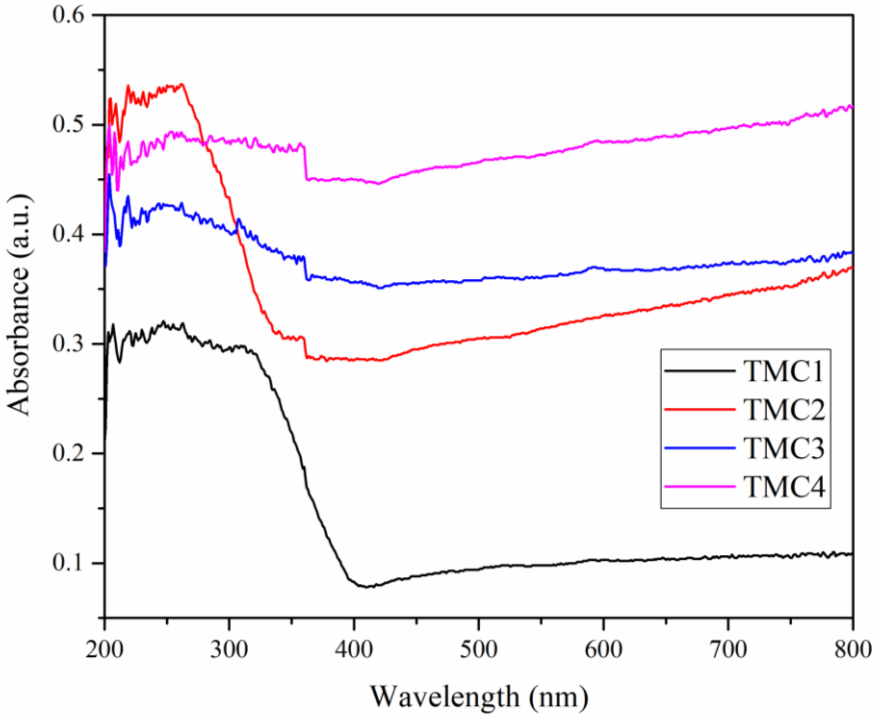

Figure S5. UV-vis diffuse reflectance spectra (DRS) of the TMC1, TMC2, TMC3 and TMC4, related to **Figure 4b.**

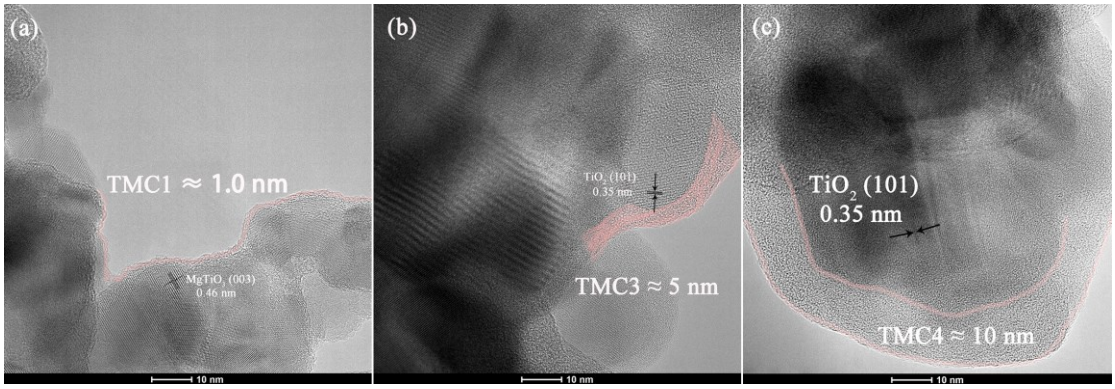

Figure S6. The HRTEM images of TMC1, TMC3 and TMC4, related to **Figure 2.** The thickness of carbon coating could be observed clearly, confirming different thickness of the carbon coating in $TiO_2/MgTiO_3/C$ samples.

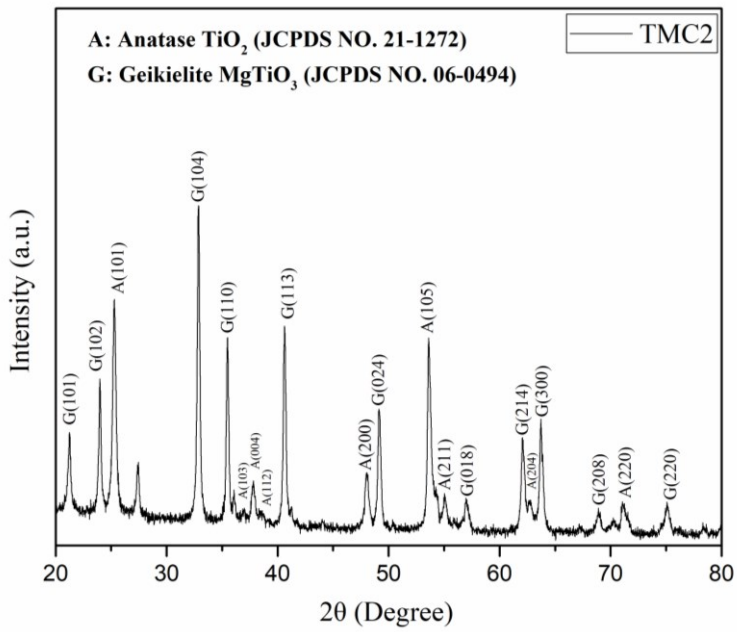

Figure S7. The XRD pattern of TMC2 sample after the fifth cycle (25 hours), related to **Figure 3b.** Figure S7 shows that the composition and crystal structure of the TMC2 sample do not change, indicating that the as-prepared photocatalysts have good optical stability. The slight reduction of the performance mainly comes from the consumption of sacrificial agent or the adverse reaction.

Table S1. Experimental recipe of TMC series and the corresponding results, related to **Figure 2.**

Name	$TiO_2/MgTiO_3$ (Weight ratio)	TiO_2 (g)	MCB[i] (g)	Mg [i] (g)	Ti/Mg Atomic ratio [ii]
TMC1	9:1	1.0	0.12	0.05	9:1
TMC2	7:3	1.0	0.4	0.15	4:1
TMC3	5:5	1.0	0.6	0.24	3:1
TMC4	3:7	1.0	0.85	0.34	10:7

MCB: $Mg(OH)_2{\cdot}4MgCO_3{\cdot}5H_2O$; [i]: determined by the desired addition based on the above reaction formula; [ii]: determined by TEM-EDS;

Table S2. The unit cell parameters of TMC samples calculated by software Jade 6.5, related to **Figure 1.**

Name	TiO_2 (a=b, Å)	TiO_2 (c, Å)	$MgTiO_3$ (a=b, Å)	$MgTiO_3$ (c, Å)
TMC1	3.7862	9.5185	5.0534	13.8934
TMC2	3.7826	9.5129	5.0565	13.8974
TMC3	3.7823	9.5148	5.0544	13.8940
TMC4	3.7856	9.5033	5.0522	13.8951
Anatase TiO_2 JCPDS No. 21-1272	3.7852	9.5139	-	-
Geikielite $MgTiO_3$ JCPDS No. 06-0694	-	-	5.054	13.898

Transparent Methods

Materials

Titanium oxide (TiO_2, Degussa P-25) were bought from Sinopharm Chemical Reagent Co., Ltd, P. R. China. Magnesium carbonate basic ($Mg(OH)_2{\cdot}4MgCO_3{\cdot}5H_2O$, AR) was purchased from Shanghai Macklin Biochemical Co., Ltd, P. R. China. Magnesium Powder (Mg, 99.9%) was obtained from Shanghai Longxin Technology Development Co., Ltd, P. R. China. Hydrochloric acid (HCl, AR) was purchased from Xilong Scientific Co., Ltd, P. R. China. All materials used in this research were used without further purification. Ultrapure water was used throughout this study.

Preparation of TiO_2/$MgTiO_3$/C heterostructures

A typical synthesis process was as follows: First, 1.0 g of TiO_2 were added to different amount of $Mg(OH)_2{\cdot}4MgCO_3{\cdot}5H_2O$ matrix salt and metal Mg (99.9 %) in an agate mortar (The stoichiometric ratio based on the following reaction formula, as shown in Tab. S1), then the mixture was ground for 1 hour at room temperature. Second, the obtained samples were placed in a corundum crucible and inserted into a tubular furnace, annealed at 550 ℃ under Ar atmosphere for 10 h, and subsequently cooled to room temperature. The mixtures were subjected to ultrasonic washing with 0.1 mol/L HCl and filtration, repeated it for several times until pH < 7 making sure the by-product MgO had been washed off. Then the products were washed with ultrapure water over and over until Cl^- ions cannot be detected and vacuum dried at 70 °C overnight in a drying oven. Based on the different weight ratio of TiO_2/$MgTiO_3$ (9:1,

7:3, 5:5, 3:7), the samples were labeled as TMC1, TMC2, TMC3 and TMC4, respectively. The corresponding process conditions are listed in Table S1.

The reaction process can be divided to three steps:

$$(MgCO_3)_4 \cdot \mathrm{Mg(OH)_2} \cdot 5\mathrm{H_2O} \rightarrow 5\mathrm{MgO} + 6\mathrm{H_2O} + 4\mathrm{CO_2}$$

$$\mathrm{TiO_2} + \mathrm{MgO} \rightarrow \mathrm{MgTiO_3}$$

$$\mathrm{CO_2} + 2\mathrm{Mg} \rightarrow \mathrm{C} + 2\mathrm{MgO}$$

The integral reaction formula can be represented as following:

$$(MgCO_3)_4 \cdot \mathrm{Mg(OH)_2} \cdot 5\mathrm{H_2O} + 5\mathrm{TiO_2} + 8\mathrm{Mg} \rightarrow 5\mathrm{MgTiO_3} + 4\mathrm{C} + 8\mathrm{MgO} + 6\mathrm{H_2O}$$

Characterization

Powder X-ray diffraction (XRD) patterns of the samples were performed at room temperature by a Bruker D8 Advance X-ray diffractometer with Cu Kα (λ = 0.15406 nm). The transmission electron microscopy (TEM) images and high-resolution transmission electron microscopy (HRTEM) images were obtained by using a Tecnai G2 F30 S-TWIN high-resolution transmission electron microscope, using an acceleration voltage of 200 kV. UV-vis diffuse reflectance spectra (DRS) was carried out using a Perkin Elmer Lambda 950 spectrometer equipped with an integrated sphere attachment in the range from 200 to 800 nm. X-ray photoelectron spectroscopy (XPS) data were obtained with an ESCA Lab 250 electron spectrometer from VG Scientific using an aluminum Kα X-ray radiation source (h = 1486.6 eV). The binding energies were referenced to the C 1s line at 284.8 eV from adventitious carbon. The photoluminescence (PL) spectra was measured at room temperature on a F-4600 FL

fluorescence spectrophotometer using a 325 nm excitation light. Raman spectroscopy was conducted using a Raman microscope (Renishaw in via microscope equipped with 488 nm Ar ion laser and a grating of 2400 L/mm) with a spectral resolution of < 1 cm^{-1}. The specific surface area (BET) was measured with a 3H-2000PS2 instrument, using the adsorption of N_2 at the temperature of liquid nitrogen.

Photocatalytic hydrogen production

Photocatalytic hydrogen production was conducted on an online photocatalytic hydrogen production system (PerfectLight, Beijing, China, Labsolar-ⅢAG). A full spectrum solar simulator (Perfectlight, Beijing, China, PLS-SXE300) with AM 1.5G filter is used as the excitation light source (Power: 1 sun light). A powder sample of the photocatalyst (0.05 g) was suspended in a mixture of 70 mL of ultrapure water and 30 mL of triethanolamine (TEOA) in the cell and treated by ultrasound for 30 min. The distance between lamp and liquid-level was about 10 cm, the irradiation area was 10 cm^2. The whole photocatalytic reaction took place at room temperature. During the photocatalytic process, vigorous magnetic stirring and cooling water were used to help the catalysts perform efficiently and to keep the system at room temperature, respectively. Pt-loaded photocatalysts were prepared by using *in situ* photo-deposition method. On this case, the photocatalyst powder was added to an aqueous TEOA solution containing the required amount (1 wt. % of Pt) of H_2PtCl_6. The high purity Ar gas at a rate of 6.0 $ml \cdot min^{-1}$, regulated by a CS200 mass flow controller (Sevenstar, Beijing, China), as a carrier gas, flowed continuously through the reactor and allowed

the hydrogen released by the photocatalytic water splitting under irradiation. The resultant gas flowed through the quantitative loop of a six-way valve to a vent, while it was tested by using gas chromatography (Fuli Instruments, Zhejiang, China, GC9790, thermal conductivity detector (TCD), 5 Å molecular sieve columns and Ar carrier) every 1 h to analyze the hydrogen content so as to determine the hydrogen production rate. The mass flow controllers and gas chromatography were calibrated before each experiment.

Photo-electrochemical measurements

Photoelectrochemical measurements (PEC) were performed in three-electrode quartz cells with a 0.5 mol/L Na_2SO_4 (pH= 6.82) electrolyte solution. Platinum mesh (2 × 3 cm^2) was used as the counter electrode, and Ag/AgCl (KCl saturated) were used as the reference electrodes. The working electrode made as: 10 mg of TMC photocatalyst and 10 ml ethanol were mixed under an ultrasonic wave for 10 min to produce a slurry, which was then spin-coated onto a 2 × 3 cm^2 ITO glass substrate. The coated layer was dried at 80 ℃ for 12 h in an electrical oven, then went through 400 ℃ calcination under Ar atmosphere for 1 h. The photoelectrochemical experiment results were recorded using an electrochemical system (Shanghai Chenhua Instruments, CHI760E). A 300 W Xe lamp (Beijing Perfectlight, PLS-SXE300) equipped with an AM 1.5G filter was used as the light source. Potentials were given with reference to the Ag/AgCl. The photo response of the samples as visible light on and off was measured at 0.0 V. Electrochemical impedance spectra (EIS) were measured at 0.0 V. A

sinusoidal ac perturbation of 5 mV was applied to the electrode over the frequency range from 0.05 to 105 Hz. The Mott-Schottky plots were obtained at a fixed frequency of 1 kHz in the dark.